Remote Sensing of Environment 335 (2026) 115293

Contents lists available at ScienceDirect

Remote Sensing of Environment

journal homepage: www.elsevier.com/locate/rse

Seasonal vertical surface thaw displacement in 2018 on Samoylov Island (Lena Delta, northeastern Siberia) measured by satellite SAR interferometry with X-, C- and L-band sensors

Tazio Strozzi [a,*], Nina Jones [a], Julia Boike [b,c], Sofia Antonova [b], Birgit Heim [b], Silvan Leinss [a], Urs Wegmüller [a], Sebastian Westermann [d], Andreas Kääb [d], Guido Grosse [b,e], Annett Bartsch [f]

[a] Gamma Remote Sensing, Gümligen, Switzerland
[b] Alfred Wegener Institute Helmholtz Centre for Polar and Marine Research, Potsdam, Germany
[c] Geography Department, Humboldt-Universität zu Berlin, Germany
[d] Department of Geosciences, University of Oslo, Norway
[e] Institute of Geosciences, University of Potsdam, Germany
[f] b.geos, Korneuburg, Austria

ARTICLE INFO

Edited by: Dr. Menghua Wang

Keywords:
Permafrost
Seasonal surface thaw displacement
Active layer
Arctic
Lena Delta
SAR interferometry
Sentinel-1
TerraSAR-X
ALOS-2 PALSAR-2

ABSTRACT

In low-land permafrost regions, the landscape can be subjected to significant seasonal cycles of vertical surface deformation. This effect is mainly driven by seasonal thaw subsidence and frost heave caused by water migration and ice-lens formation during thawing and freezing, with additional contributions from volumetric changes associated with phase transitions between ice and liquid water. Satellite differential SAR interferometry (DInSAR) has been used in the past to quantify the seasonal vertical surface displacement from thaw subsidence and frost heave. However, the DInSAR phase does not only contain information on ground displacement, but is also influenced by changes in atmospheric, soil moisture, vegetation and snow cover conditions. The aim of our study was to quantify the vertical seasonal surface thaw displacement using DInSAR with almost coinciding Sentinel-1 (C-band), TerraSAR-X (X-band) and ALOS-2 PALSAR-2 (L-band) data, to compare the results obtained at different frequencies and to relate the results to in situ displacement data and soil, moisture and land cover characteristics. As our study area we chose Samoylov Island in the Lena Delta, northeastern Siberia, which lies in the continuous permafrost zone and is characterized by ice-wedge polygons and small ponds and shallow lakes. Here, we processed satellite imagery during the snow-free period in 2018. We found rates of vertical thaw displacement of several centimeters in the north-western part of the island, a more stable region along the eastern part and heterogeneous rates of movement in the central part. In general, there is a good agreement between the magnitude and spatial patterns of the seasonal surface thaw displacement measured at different frequencies. This suggests that surface displacement is the predominant effect on the DInSAR phase compared to effects from variations in soil moisture, which should increase with wavelength as the penetration depth is greater at lower frequencies, and effects from vegetation, which should cause stronger systematic distortions at higher frequencies. Validation with in situ measurements showed that values determined remotely are smaller than those measured in situ, highlighting the challenges of accurately capturing and representing sub-pixel variability of displacements. A comparison with a detailed habitat type map illustrates that the large-scale magnitude of seasonal deformation is predominantly related to soil type and moisture conditions.

1. Introduction

In low-land permafrost areas, where the near-surface ground contains large quantities of ice and water and overlies perennially frozen ground, the terrain can experience significant seasonal deformation processes. This is primarily driven by water migration and ice-lens formation during thawing and freezing, with additional contributions from volumetric changes associated with phase transitions between ice and

* Corresponding author.
E-mail address: strozzi@gamma-rs.ch (T. Strozzi).

https://doi.org/10.1016/j.rse.2026.115293
Received 30 October 2025; Received in revised form 29 January 2026; Accepted 2 February 2026
Available online 5 February 2026

liquid water (French, 2007; Günther et al., 2015; Ballantyne, 2018). Annually, surface displacement includes both a downward movement of the land surface associated with the seasonal thaw in summer (subsidence) and an upward movement that occurs during the frost period in autumn and winter (uplift). Substantial displacement due to thawing and freezing of ground ice may indirectly indicate the presence of ice/water-rich soils and/or a thick active layer in the subsurface. Seasonal changes in surface elevation can reach decimeters every year (Shiklomanov et al., 2013). The magnitude of the displacement can vary from year to year, depending on the warming of the soil (expressed e.g., in Accumulated Degree Days of Thaw, ADDT) or change in water content through variations in the soil water budget. When seasonal thaw subsidence in summer exceeds in the long term over upward movement associated with frost heave in fall and winter, an effective long-term subsidence of the surface is expected. Long-term subsidence is usually explained by permafrost degradation, i.e., as an impact of changing climatic conditions, where thawing of ice-rich permafrost leads to increasing seasonal subsidence magnitudes over successive years (Shiklomanov et al., 2013; Scheer et al., 2023). However, interannual variations in the active layer can sometimes obscure permafrost thaw trends (Nyland et al., 2021). Various methods exist to observe and monitor seasonal surface deformation of the active layer, including a range of field methods, modeling, and remote sensing, with a recent review of available observaitons pointing at an overall trend of long-term thaw subsidence in the Northern Hemisphere (Streletskiy et al., 2025). Developing satellite-based methods to accurately and systematically track seasonal thaw subsidence is essential to also quantify long-term changes and permafrost degradation across large regions.

Satellite Differential Synthetic Aperture Radar Interferometry (DInSAR) has played a crucial role in quantifying surface displacement over low-lying permafrost regions during thawing seasons (Liu et al., 2010; Short et al., 2014; Daout et al., 2017; Strozzi et al., 2018; Rouyet et al., 2019; Chen et al., 2020; Rouyet et al., 2021). Additionally, it has been employed to derive remotely-sensed seasonal changes in active layer depth (Schaefer et al., 2015; Wang et al., 2018; Zhang et al., 2020) and map frost susceptibility areas (Scheer et al., 2023). Seasonal as well as year-to-year developments in the freeze-thaw cycle and subsequent subsidence have been identified using DInSAR data from various satellite missions (Short et al., 2011; Wang et al., 2017; Antonova et al., 2018; Bartsch et al., 2019; Michaelides et al., 2021). It is important to note that the sensitivity of the phase to displacement diminishes with decreasing radar frequency. For example, a complete phase cycle (i.e., a "fringe") corresponds to a deformation of about 3 cm at C-band, 1.5 cm at X-band and 12 cm at L-band. While the DInSAR phase is routinely used to estimate surface displacements, it is also influenced by changes in atmospheric, soil moisture, vegetation and snow cover conditions (De Zan et al., 2014; Ansari et al., 2021).

Phase distortions caused by spatially heterogeneous tropospheric (in particular water vapor) and ionospheric conditions limit the accuracy of DInSAR (Hanssen, 1998). Numerous methods were developed to systematically compensate for the tropospheric and ionospheric phase components in interferograms. For instance, stacking of interferograms can improve the ratio between the displacement signal and the atmospheric phase errors (Sandwell and Price, 1998). Algorithms based on the combination of numerous DInSAR images to derive deformation time series were also used to identify and filter out atmospheric phase artifacts (Berardino et al., 2002). A further method involved utilizing external information on atmospheric conditions (Xiao et al., 2021). The split-spectrum method, based on the dispersive nature of the ionosphere, was applied at L-band to correct for the ionospheric component of the interferometric phase (Gomba et al., 2016). Because cold air cannot hold a lot of water vapor and convection is less pronounced (Hanssen, 1998), for small-scale permafrost related applications, e.g., with an area size <5 km^2, low-pass filtering can be also used to estimate the atmospheric phase screen (Strozzi et al., 2018; Michaelides et al., 2021). Elevation-correlated tropospheric delays are not taken into account in this study because the study area is flat.

A slow increase in soil moisture has been found to correspond to an interferometric phase that is associated with surface subsidence, i.e., apparent movement away from the satellite (Nolan et al., 2003; Morrison et al., 2011; De Zan et al., 2014; Zwieback et al., 2017; Eshqi Molan and Lu, 2020). The phase velocity of the electromagnetic waves decreases as the soil gets moister, corresponding to an increase in the optical path. On the contrary, slow drying results in an apparent motion towards the satellite, which can be perceived as ground uplift. Variations in soil moisture can typically change the phase by up to about 0.5π, corresponding to a spurious displacement of about $\lambda/8$, i.e., around 10–20% of the radar wavelength. Additionally, the magnitude of the signal is expected to increase with the wavelength, because the penetration grows faster than the wavelength at lower frequencies. Most soils have a relatively high permittivity, therefore, phase disturbances are often negligible in terms of contribution to the perceived displacement in the satellite line-of-sight (LOS). In practice, for bare soils the measured backscattered signal at L- to X-band is commonly attributed to the rough surface. Additionally, if between the two satellite passes the soil wetness increases so that the phase center changes, a decrease of the degree of coherence (in short coherence) is expected. The phase effect becomes noticeable only for slightly wet sand or remnant moisture in grassroots in dry sand.

Biomass growth introduces an additional range delay or phase excess, with an apparent motion away from the satellite (Westerhoff and Steyn-Ross, 2020; Ansari et al., 2021). Phase disturbances are most sensitive to changes in vegetation height and moisture. Vegetation height changes of a few tens of centimeters can lead to phase disturbances of several tens of degrees (Brancato and Hajnsek, 2018). Consequently, these disturbances contribute to significant noise to the perceived LOS displacement. Additionally, a vegetation layer can lead to a decrease or even complete loss of the coherence, in particular at higher frequencies (Wegmuller and Werner, 1997).

Refraction of microwaves in dry snow has a significant effect on the interferometric phase (Guneriussen et al., 2001). For dry snow, a direct relationship between changes in Snow Water Equivalent (SWE) and the DInSAR phase exists. A decrease in SWE reduces the range delay, with an apparent motion towards the satellite, while an increase in SWE increases the range delay, with an apparent motion away from the satellite. Even small changes in SWE, which may be caused by snowfall or snowdrift between the radar image acquisitions, can introduce significant interferometric phase delays. For instance, for a snow density of 0.2 g/cm and an incidence angle of 23°, phase wrapping occurs for a change in snow depth of 2.9 times the wavelength, which is equivalent to a change in snow depth of 16 cm at C-band, 9 cm at X-band and 74 cm at L-band (Guneriussen et al., 2001). Therefore, already small spatial variations of snow depth can cause a rapid loss of coherence, in particular at higher frequencies (Sarabandi and Azadegan, 2000). Wet snow metamorphism also causes a strong decrease of the coherence (Strozzi et al., 1999). The coherence over the typically moist, vegetated and snow-covered low-land permafrost areas is thus also a critical factor for a successful estimation of the seasonal surface thaw displacement (Antonova et al., 2018). The lower frequencies can assure longer temporal baselines, in particular in case of vegetation and snow cover changes (Short et al., 2011). The wavelength also governs the sensitivity to roughness and penetration depth, which suggests a possible impact on the soil moisture effects.

In order to bridge the existing research gap in understanding the influence of varying atmospheric, soil moisture, vegetation and snow cover conditions on the assessment of seasonal surface thaw displacement in permafrost regions, we analyzed a series of satellite SAR imagery from three different sensors acquired between June and September 2018 over the central part of the Lena Delta. The data set included C-Band from Sentinel-1, X-Band from TerraSAR-X and L-band from ALOS-2 PALSAR-2. In this contribution, we first discuss the effect of the coherence for the interferometric processing of DInSAR data in

series with nominal repeat cycles of 12 days (Sentinel-1), 11 days (TerraSAR-X) and 14/42 days (ALOS-2 PALSAR-2). We then present and compare the seasonal surface thaw displacement maps derived from the different sensors, validate the satellite derived information with in situ measurements (Boike et al., 2019) and compare the displacement maps to a detailed habitat type map (Lisovski et al., 2025).

2. Site and data

2.1. Samoylov Island (Lena Delta)

Samoylov Island is located in the central part of the Lena Delta at the Laptev Sea coast in northeastern Siberia in the zone of continuous permafrost (Boike et al., 2013; Boike et al., 2019; Obu et al., 2019). The Lena Delta consists of three geologically and geomorphologically diverse terrace complexes (Schwamborn et al., 2002; Morgenstern et al., 2011; Morgenstern et al., 2013), covered with tundra vegetation and active floodplains (Fig. 1). Because of its broad landscape and habitat diversity the delta is a biodiversity hotspot and was designated a State Nature Reserve in 1995. With an area of about 32,000 km^2, the Lena Delta is the largest delta in the Arctic and one of the largest in the world (Are and Reimnitz, 2000). The delta comprises more than 1500 islands of various sizes, which are divided by small and large river channels.

Samoylov Island is part of the first delta terrace. It covers an area of about 5 km^2 and is dominated by wet polygonal tundra. Samoylov Island consists of a Holocene river terrace (Kartoziia, 2019; Polyakov et al., 2022), with ice-rich polygonal tundra characterized by low-centered ice wedge polygons to the east and a large sandy floodplain to the west (Fig. 2). Grasses, hydrophytic sedges as well as mosses dominate the vegetation in the wet polygon centers and on their edges. Mesophytic dwarf shrubs and mosses dominate the polygon rims. The research station Samoylov Island (72.370 N 126.475 E), located in the southwestern part, offered the possibility to serve as a base for long-term permafrost monitoring in Russian-German cooperation and regular in situ measurements (Boike et al., 2013).

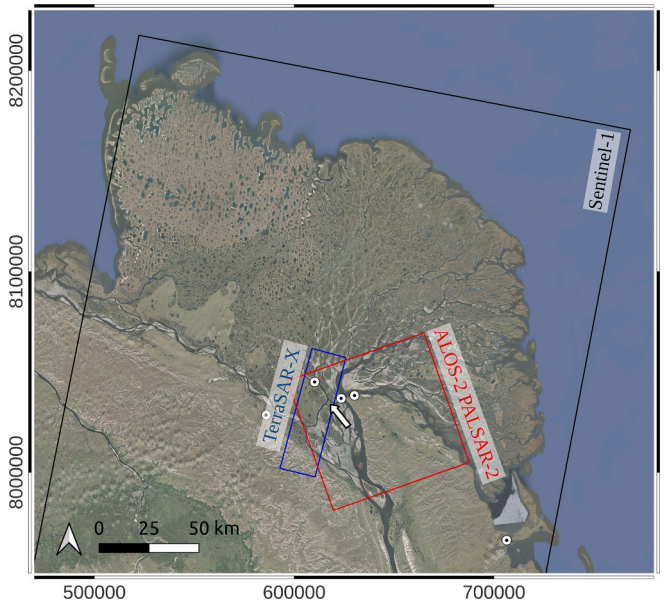

Fig. 1. Footprints of the Sentinel-1 (black), TerraSAR-X (blue) and ALOS-2 PALSAR-2 (red) images over the Lena Delta located at the Laptev Sea coast in Northeast Siberia. The arrow indicates the location of Samoylov Island (for Google image and habitat classes see Fig. 3). Stable targets are shown with white dots, from left to right: barren, exposed surface Nr. 1, Amerika Khaya, Stolb Island, barren, exposed surface Nr. 2 and Tiksi airport. Background image is Bing Aerial (©Microsoft). (For interpretation of the references to color in this figure legend, the reader is referred to the web version of this article.)

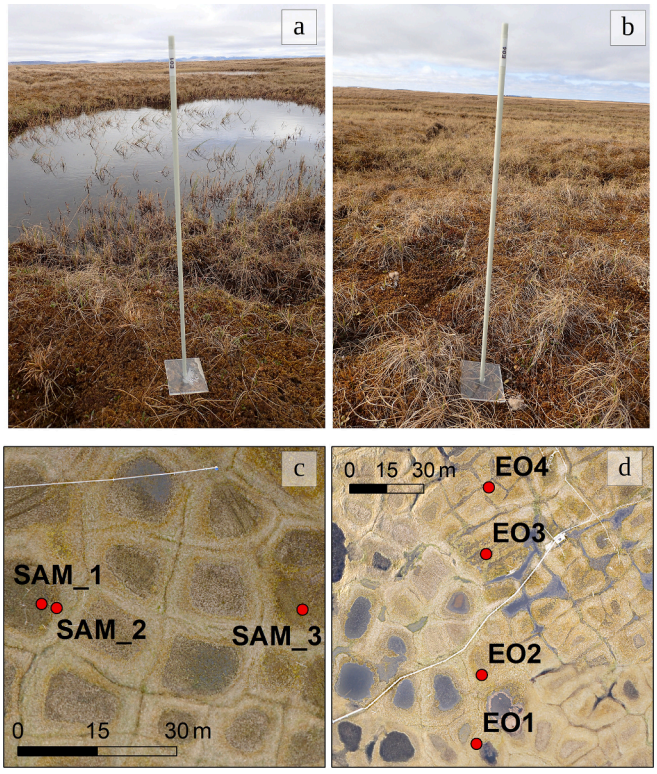

Fig. 2. Photographs of two benchmark poles within the typical polygonal tundra landscape on the Holocene terrace covering the eastern part of Samoylov Island with grasses, hydrophytic sedges and mosses: (a) EO1 and (b) EO4. The positions of the three metal pipes SAM_1 to SAM_3 (c) and of the four fiberglass poles EO1 to EO4 (d) are shown on a summer 2015 aerial RGB orthomosaic (Boike et al., 2015). The typical size of ponds is on the order of several meters.

The climate in the Lena Delta features long, extremely cold winters and short, cool summers. For the period from 1998 to 2017, the mean annual air temperature was −12.3 °C, with the mean monthly temperature of the warmest month (July) being 9.5 °C and the coldest month (February) being −32.7 °C (Boike et al., 2019). The regional arctic-continental climate allows maximum thaw depths of about 0.5 m. The depth of zero annual amplitude (i.e., temperature fluctuations <0.1 K) is at 20.75 m. At this depth, the temperature has increased from −9.1 °C in 2006 to −7.7 °C in 2017 (Boike et al., 2019). The average annual rainfall between 1998 and 2017 was 169 mm. Snow usually starts to accumulate in September, starts to melt in May and is typically gone in less than a month. Snow depth can significantly vary depending on topography and wind action with (mean) snow depths of 17 cm on the polygon rims and about 46 cm in the polygon centers. In some more recent years snow depth reached up to 70 cm.

2.2. SAR data

Our work is largely driven by satellite data availability. We could perform the cross-comparison between Sentinel-1, TerraSAR-X and ALOS-2 PALSAR-2 data only for the period from June to September 2018 (Table 1), as this time frame represented the sole summer season during which ALOS-2 PALSAR-2 data were consistently acquired over Samoylov Island. In other years, ALOS-2 PALSAR-2 data were sporadic and unsuitable for DInSAR time series analyses. The footprints of the Sentinel-1, TerraSAR-X and ALOS-2 PALSAR-2 images are shown in Fig. 1. The area with overlapping acquisitions from all three sensors covers a small section of the Lena Delta, including Samoylov Island.

Sentinel-1 SAR observations (Torres et al., 2012) follow a baseline, pre-defined mission observation scenario. Regular acquisitions in the Interferometric Wide (IW) swath mode are available along the

Table 1
Satellite SAR data with indication of perpendicular baseline and acquisition time interval. The vertical displacement normalization factor is used to convert LOS to vertical displacement. The seasonal deformation amplitude normalization factor is considered to adjust for any additional displacement occurring outside the time span of the temporally coherent DInSAR stack (Scheer et al., 2023).

Sensor	Date 1	Date 2	Perpendicular baseline (m)	Temporal baseline (days)	Vertical displacement normalization factor (incidence angle)	Seasonal deformation amplitude normalization factor
Sentinel-1	2018.06.12	2018.06.24	−42.4	12	1.27 (38.27°)	1.42
	2018.06.24	2018.07.06	−68.2	12		
	2018.07.06	2018.07.18	−50.1	12		
	2018.07.18	2018.07.30	69.5	12		
	2018.07.30	2018.08.11	92.5	12		
	2018.08.11	2018.08.23	−72.5	12		
	2018.08.23	2018.09.04	−30.4	12		
	2018.09.04	2018.09.16	−11.4	12		
TerraSAR-X	2018.06.18	2018.06.29	−27.1	11	1.17 (31.65°)	1.61
	2018.06.29	2018.07.10	7.5	11		
	2018.07.10	2018.07.21	−95.5	11		
	2018.07.21	2018.08.01	−15.9	11		
	2018.08.01	2018.08.12	15.7	11		
	2018.08.12	2018.08.23	91.4	11		
	2018.08.23	2018.09.03	−109.5	11		
	2018.09.03	2018.09.14	−68.6	11		
ALOS-2 PALSAR-2	2018.06.12	2018.07.24	−96.8	42	1.24 (36.34°)	1.42
	2018.07.24	2018.09.04	117.5	42		
	2018.09.04	2018.09.18	−32.3	14		

descending orbit every 12 days, with 8 images acquired between 12 June and 16 September 2018 at VV polarization (Table 1). The Sentinel-1 IW frame is 250 km wide and has an incidence angle at Samoylov Island of 38.27°. C-band Sentinel-1 data have a center frequency of 5.4 GHz (wavelength 5.6 cm) and a 5 × 20 m (slant-range x azimuth) spatial resolution.

TerraSAR-X data (Pitz and Miller, 2010) are tasked by the German Aerospace Center (DLR) every 11 days over the central Lena Delta. In this study we considered 8 images acquired along the descending orbit between 18 June and 14 September 2018 at HH polarization (Table 1). The TerraSAR-X StripMap frame is 30 km wide, with an incidence angle at Samoylov Island of 31.65°. X-band TerraSAR-X data have a center frequency of 9.6 GHz (wavelength 3.1 cm) and a 1 × 3 m spatial resolution.

Four ALOS-2 PALSAR-2 Stripmap Fine data (Suzuki et al., 2013) acquired at HH polarization between 12 June and 18 September 2018 with time intervals of 42/42/14 days along the ascending orbit were analyzed (Table 1). The ALOS-2 PALSAR-2 StripMap frame is 70 km wide, with an incidence angle at Samoylov Island of 36.34°. L-band ALOS-2 PALSAR-2 data have a center frequency of 1.2 GHz (wavelength 24.3 cm) and a 9 × 5 m spatial resolution.

For topographic phase removal and terrain corrected geocoding we use the TanDEM-X Digital Elevation Model (DEM). The TanDEM-X DEM is based on satellite TanDEM-X SAR acquisitions from December 2010 to early 2015 and the product is provided with a pixel spacing of approximately 12 m (Zink and Moreira, 2014). GPS comparisons prove an absolute vertical mean error smaller than ±0.20 m, a Root Mean Square Error (RMSE) smaller than 1.4 m and an absolute 90% linear height error below 2 m (Wessel et al., 2018). The RMSE values are sensitive to land cover types, for low vegetation the RMSE is ±1.1 m.

2.3. Stable targets

To derive the absolute displacement values from the DInSAR measurements, several stationary locations – so-called stable targets - were considered (Fig. 1). In the central Lena Delta, we identified two locations with elevated barren bedrock exposures: Amerika Khaya (72.476 N 126.281 E) and Stolb Island (72.396 N 126.660 E). We are not aware of other bedrock outcrops in the Lena Delta itself, but there are several areas with exposed bedrock along the southern margin on the mainland side. Additionally, we therefore considered two barren, exposed surfaces with rock rubble at 72.405 N 126.860 E and 72.339 N 125.537 E, as well as the airport near Tiksi (71.706 N 128.898 E). Alternative stable targets could include the sandy sediments in floodplain areas, where the freeze/thaw deformation is expected to be minimal (Liu et al., 2010). We did not consider such locations, however, as it is unclear to what extent and over which time periods deposition/erosion occurs.

2.4. Field data

Quantifying surface displacement in situ is notoriously difficult due to the small size of the displacement (on the order of cm), the high heterogeneity of the landscape, and the lack of suitable automated and accessible ground-based technology. Surface displacement was surveyed on Samoylov Island by manually measuring the above-ground part of several benchmark poles, all anchored deep into the permafrost. Each pole was equipped with a plexiglass plate that was threaded through the pole and rested on the ground surface (Fig. 2a and b). This design provided a stable reference point on the ground while minimizing the influence of vegetation on the measurements. Three metal pipes (SAM_1 to SAM_3, Fig. 2c) and four fiberglass poles (EO1 to EO4, Fig. 2d) were installed on Samoylov Island (Fig. 3a). The measurements were carried out on 16–17 June 2018 and again on 7 September 2018, effectively capturing the primary period of seasonal thaw. For a detailed description of the in situ setup, refer to Antonova et al. (2018). Overall, a measurement uncertainty of the in situ data of ±1 cm is assumed.

The Samoylov Permafrost Observatory (Boike et al., 2013, 2018, 2019, 2022) is set up to record further in situ data on Samoylov Island, providing continuous time series on air temperature, ground temperature, snow depth, water level above the surface, thaw depths of the active layer and time-lapse camera observations. In the context of a long-term record, environmental conditions in spring and summer 2018 on Samoylov Island were not unusual, representing a normal year in terms of spring temperatures, timing of snow melt and timing of river ice break-up (Boike et al., 2019; Heim et al., 2022; Juhls et al., 2020). The first consecutive days of positive mean air temperature were recorded on 22 May 2018, while the first consecutive days of negative mean air temperature were recorded on 29 September 2018. The ground surface started to warm above 0 °C on 1 June 2018 at polygon center and on 10 June 2018 at polygon edge. Snow cover maximum thickness in March to May 2018 before snow melt was 30 cm. The land surface became snow free from late May to beginning of June and the duration of the snow free period lasted until 10 October 2018. After the ice break-up at the end of May 2018, the spring discharge maximum and subsequent

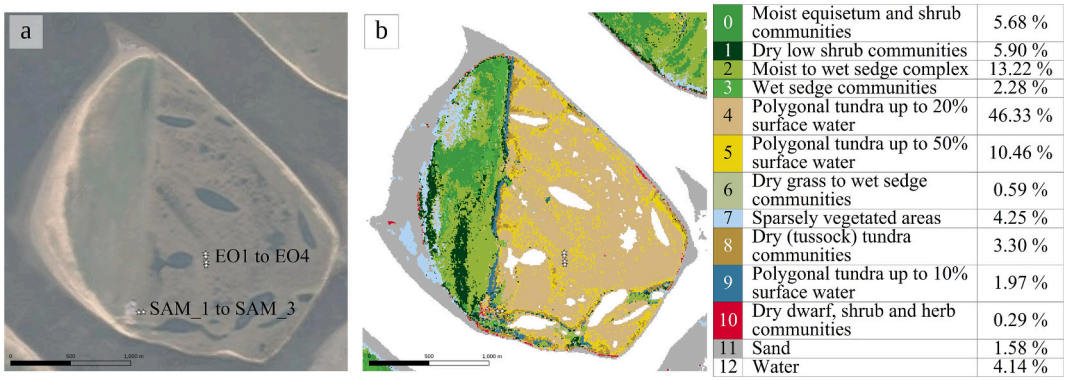

Fig. 3. (a) Google image of Samoylov Island. The white stars indicate the locations of in situ surface displacement measurements. (b) Habitat classes (Lisovski et al., 2025) on Samoylov Island. The coverage in % of each habitat class within the island is indicated in the color legend.

flooding of the river floodplain occurred about four days later. Snow cover melt and spring flood were thus not interacting with the DInSAR analyses of the three sensors starting in mid June 2018.

The highest water level above the surface occurred after snow melt in late May and early June 2018, followed by surface drying in June. Surface wetting occurred again in July, followed by a renewed drying in August and September. Surface drying in this context refers to the water level falling below the ground surface due to the hydrology of the polygons in summer. The thaw depth of the active layer on 20 June 2023 averaged 19 cm on the grid of the Circumpolar Active Layer Monitoring (CALM) covering polygonal tundra on wet polygons and dry ridges, with mainly only the moss layer thawing (Boike et al., 2019). Thereafter, the thaw migrated through the soil and reached an average of 56 cm on 14 September 2023. In terms of June temperature and vegetation greening, 2018 stands out as the year with the highest monthly temperature in the Samoylov long-term temperature record (Boike et al., 2022) and very strong vegetation emergence recorded by a time-lapse camera close to the ground (Morgenstern et al., 2021; Heim et al., 2022). In particular, the time-lapse camera showed leaf out of shrubs in mid-May 2018 during snow cover, greening of graminoids in late May 2018 with snow melt and patchy snow cover and sprouting of vascular plants in mid-June 2018. Further time-lapse camera monitoring from the top of the Samoylov station (data not published) showed a mud-covered floodplain from the spring flood in early June, with graminoids greening in early June.

2.5. Habitat class map

A new map of the habitat classes observed in the Lena Delta provides the baseline against which future observations can be compared (Lisovski et al., 2025). This land cover map was produced using aggregated summer 2018 Sentinel-2 satellite spectral data trained from a wide range of in situ vegetation plots (plant composition, biomass and hyperspectral field measurements). Eleven distinct habitat classes linked to different vegetation compositions were defined. On Samoylov Island (Fig. 3b), *Moist equisetum and shrub communities* (class number 0), *Moist to wet sedge complex* (class number 2) and *Wet sedge communities* (class number 3) are predominantly present on the floodplain in the West. *Dry low shrub communities* (class number 1) cover the drier ridges in the southwestern part of the floodplain. The Holocene terrace that builds up the eastern part of Samoylov Island is dominated by *Polygonal tundra up to 50% surface water* (class number 4) and *Polygonal tundra up to 20% surface water* (class number 5).

3. Methodology

We derived the seasonal vertical surface thaw displacement in 2018 at Samoylov for Sentinel-1 (C-band), TerraSAR-X (X-band) and ALOS-2 PALSAR-2 (L-band) SAR data using differential interferometry methods (DInSAR). Two SAR images covering the same area and acquired at different times are combined to measure their phase difference (Bamler and Hartl, 1998; Rosen et al., 2000). After removal of the topographic phase component, this reflects surface movement in the LOS, with atmospheric disturbances as the major limitation. Wrapped interferograms show LOS displacement as phase cycles of a 2π ambiguity, which can be converted to absolute values through phase unwrapping procedures. We generated multiple interferograms in series with the shortest possible temporal baselines for each sensor to derive consistent time series of displacement within the summer season of 2018 (Table 1).

3.1. Sentinel-1

The Sentinel-1 processing sequence includes the following steps. First, a reference SLC is selected and geocoded to the available TanDEM-X DEM. All other SLC images are co-registered to the reference in radar geometry with a refinement based on the spectral diversity within bursts and swaths (De Zan and Monti-Guarnieri, 2006). Interferograms are generated with a multi-looking factor of 5 pixels in slant-range and 1 pixel in azimuth from SLC image in series, i.e., following the daisy chain approach A-B, B-C, C-D, etc. (Supplementary Fig. 1). Good coherence is observed from 12 June 2018 onwards. In order to smooth out phase noise, adaptive filtering based on the power spectral density is applied (Goldstein and Werner, 1998). The filtered interferograms are then unwrapped with a minimum cost flow algorithm (Costantini, 1998) to derive absolute displacement values in meters. Any remaining local unwrapping errors are corrected individually through manual ambiguity corrections based on a visual check of residues of phase unwrapping. To remove noisy and decorrelated areas, a mask is determined on the basis of the average 12-days coherence and average 12-days filtered interferogram correlation coefficient. The resulting noise-filtered and unwrapped, continuous interferograms are inverted to derive phase time series of LOS displacement occurring from June to September 2018 (Berardino et al., 2002; Werner et al., 2012). Maximum surface thaw displacement is observed with the acquisition of 16 September 2018; subsequent satellite data show no further significant increase in subsidence. An additional low-frequency correction is applied to the resulting displacement map to smooth atmospheric disturbances. To ensure that our spatial filter does not remove signals originating from Samoylov Island (area ~ 5 km^2), we set a filter radius of 512 range samples, corresponding to approx. 9700 m.

To calibrate the Sentinel-1 LOS displacement, five locations assumed to be stationary were considered as stable targets. After a first calibration through best fit of the LOS displacements at these locations (i.e., using a linear regression), results show that the barren bedrock exposure at Stolb Island is subject to large subsidence outside the margin of error. This may be due to the fact that the central upper part of the island is

covered by weathered bedrock with some soil on top. This location was therefore excluded from the calibration, which was thus conducted only with the remaining four targets. The calibrated LOS displacement is then converted to vertical displacement, using the sensor incidence angle of 38.27° and a factor of 1.27. Such an approximation is based on the assumption that displacement is predominantly in the vertical direction and is valid in flat areas devoid of significant topographic relief. The final vertical summer 2018 displacement is normalized to adjust for any additional displacement occurring outside the time span of the temporally coherent DInSAR stack. Following Scheer et al. (2023), we use Accumulated Degree-Days of Thawing (ADDT) from the Samoylov station (Boike et al., 2019) to scale the partial-season DInSAR displacement to a full-season estimate. ADDT, the sum of daily mean temperatures above 0 °C, is normalized over the thawing season (Normalized Accumulated Degree Days of Thawing, NADDT) and approximates the seasonal progress of thaw. Assuming seasonal displacement grows roughly with the square-root of ADDT, the fraction of the seasonal amplitude captured between the first (tfirst) and last (tlast) SAR acquisitions is proportional to $\sqrt{\text{NADDT(tfirst)}} - \sqrt{\text{NADDT(tlast)}}$. We therefore obtain the corrected seasonal amplitude by dividing the partial-season displacement by this fraction. For Sentinel-1 in 2018, this resulted in a normalization factor of 1.42. This factor is applied uniformly over the island; spatial variability in near-surface microclimate is not resolved by our normalization as only one temperature record is available in our study region (Boike et al., 2019). The seasonal thaw displacement map is finally geocoded to the available TanDEM-X DEM.

3.2. TerraSAR-X

TerraSAR-X processing underwent largely the same sequence as applied for Sentinel-1 data. Here we generated eight continuous interferograms from June to September 2018 with a temporal baseline of 11 days and a multi-looking factor of 5 pixels in slant-range and azimuth (Supplementary Fig. 2). Coherent SAR images are observed from 18 June 2018, with maximum subsidence occurring by 14 September 2018. This allowed an almost congruent comparison with the Sentinel-1 and ALOS-2 PALSAR-2 images. Different to Sentinel-1, a quadratic polynomial phase model is subtracted from the phase time series of LOS displacement to mitigate atmospheric disturbances. The phase bias is determined with respect to Sentinel-1 values at Samoylov Island, due to an insufficient number of stable targets within the TerraSAR-X frame (Fig. 1), by setting the average difference between the values of the two sensors to zero. The resulting time series is converted to normalized vertical displacement using a factor of 1.18, based on the sensor incidence angle of 31.65°. The normalization for the seasonal deformation amplitude is based on a factor of 1.61, derived from temperature data and NADDT.

3.3. ALOS-2 PALSAR-2

Four ALOS-2 PALSAR-2 acquisitions are available over the study area in summer 2018 from 12 June to 18 September, resulting in three continuous interferograms with temporal baselines of 14 and 42 days (Supplementary Fig. 3). A multi-looking factor of 2 pixels in slant-range and 4 pixels in azimuth is applied. Processing is very similar to Sentinel-1 and TerraSAR-X, with one major difference: differential interferograms are generated with an ionospheric mitigation by means of a split-spectrum method (Gomba et al., 2016). Subsequently, adaptive filtering using the power spectral density is applied and a quadratic polynomial phase model subtracted. After phase unwrapping, the LOS phase time series is again spatially filtered across a radius of 512 range samples, corresponding to approx. 7858 m, and the phase bias determined with respect to Sentinel-1 values at Samoylov Island. The normalized vertical displacement is calculated using a factor of 1.24, based on the sensor incidence angle of 36.34°. The normalization for the seasonal deformation amplitude is calculated using a factor of 1.42, derived from temperature data and NADDT.

4. Results

4.1. Coherence

We computed the coherence over a window size of 7 × 7 pixels for all combinations of Sentinel-1, TerraSAR-X and ALOS-2 PALSAR-2 differential SAR interferograms of the thawing season 2018 and plotted it as a function of the time interval for Samoylov Island in Fig. 4. In addition, we computed the filtered interferogram correlation coefficient using an adaptive approach with a smallest correlation average box size of 3 and a largest box size of 11 (Wegmüller and Werner, 1995) for all combinations of filtered interferograms. This is also plotted in Fig. 4. The decrease in coherence with time is particularly evident for TerraSAR-X and Sentinel-1. Therefore, in our DInSAR processing sequence we only considered interferograms with the shortest possible time intervals (cf. Section 3).

The mean coherence and the mean filtered interferogram correlation coefficient were computed from the eight Sentinel-1 interferograms over 12 days, the eight TerraSAR-X interferograms over 11 days and the four ALOS-2 PALSAR-2 interferograms over 42/14 days used in our study and are presented in Fig. 5. To mask out noisy and decorrelated areas from the Sentinel-1 seasonal thaw displacement map, thresholds above 0.8 for the mean coherence and above 0.6 for the mean filtered interferogram correlation coefficient were used. For TerraSAR-X, we used thresholds above 0.8 and above 0.5, respectively. For ALOS-2 PALSAR-2, we only considered the mean filtered interferogram correlation coefficient and selected a threshold of 0.5.

4.2. Seasonal thaw displacement

The seasonal thaw displacement maps derived from the time series analysis with Sentinel-1 between 12 June and 16 September 2018, TerraSAR-X between 18 June and 14 September 2018, and ALOS-2 PALSAR-2 between 12 June and 18 September 2018 over Samoylov Island are shown in Fig. 6. The color code is saturated at 8 cm, with areas colored in red indicating cumulative subsidence. At all three frequencies we recognize larger rates of thaw displacement over the moist floodplain in the northwestern part of the island. The Holocene terrace in the east is found to be a more stable region, with more heterogeneous rates of motion in its central part, the most degraded part of the island with more water channels and ponds. The higher resolution of TerraSAR-X with respect to ALOS-2 PALSAR-2 and in particular Sentinel-1 results in a clearer picture despite lower coherence. Due to the independent thresholds used for the three sensors to mask out noisy and decorrelated areas (cf. Section 4.1), the spatial coverage with valid information is different in the three seasonal thaw displacement maps. The lakes are correctly masked out with TerraSAR-X and ALOS-2 PALSAR-2 but not for Sentinel-1, probably because of the lower spatial resolution of the C-band sensor. The most conservative map is that derived from ALOS-2 PALSAR-2, yet this map shows the closest spatial overlap with the habitat class map of the Lena Delta (Fig. 3b), masking out water and the large sandy floodplain to the west possibly affected by strong soil moisture variations. The ALOS-2 PALSAR-2 mask is therefore considered for the intercomparison of seasonal thaw displacement at C-, X- and L-band (cf. Section 5.3). The similar patterns of seasonal subsidence over Samoylov Island determined with three sensors also indicate the effectiveness of our atmospheric disturbance mitigation strategy, whereby we distinguish large-scale atmospheric variations on the scale of several kilometres from small-scale displacement over the island. However, the three seasonal thaw displacement maps over a larger section of the central part of the Lena Delta, presented in Supplementary Fig. 4, are less consistent. In order to work on a larger scale, suitable atmospheric filtering must be investigated (Widhalm et al., 2025).

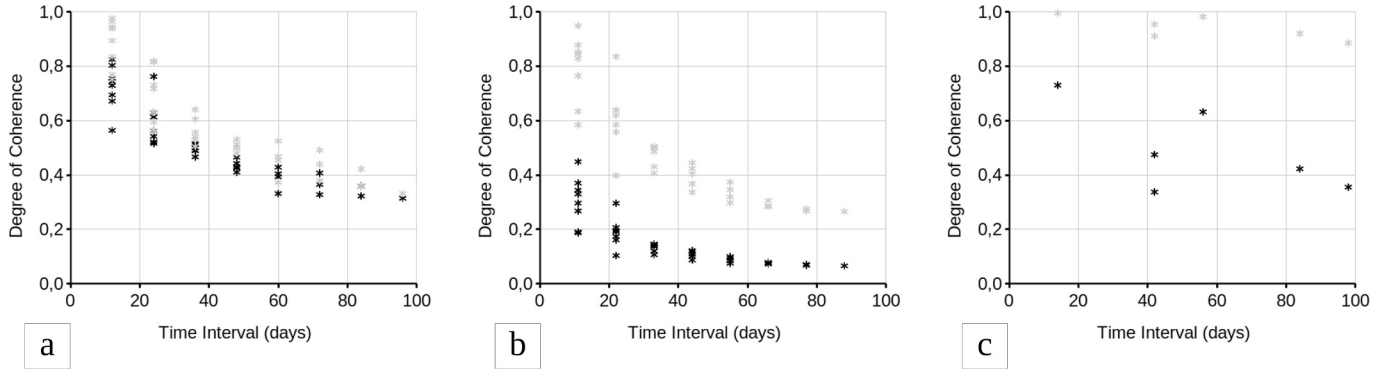

Fig. 4. Coherence (black stars) and filtered interferogram correlation coefficient (light grey stars) for Sentinel-1 (a), TerraSAR-X (b) and ALOS-2 PALSAR-2 (c) differential interferograms as a function of the time interval over Samoylov Island for the period June to September 2018.

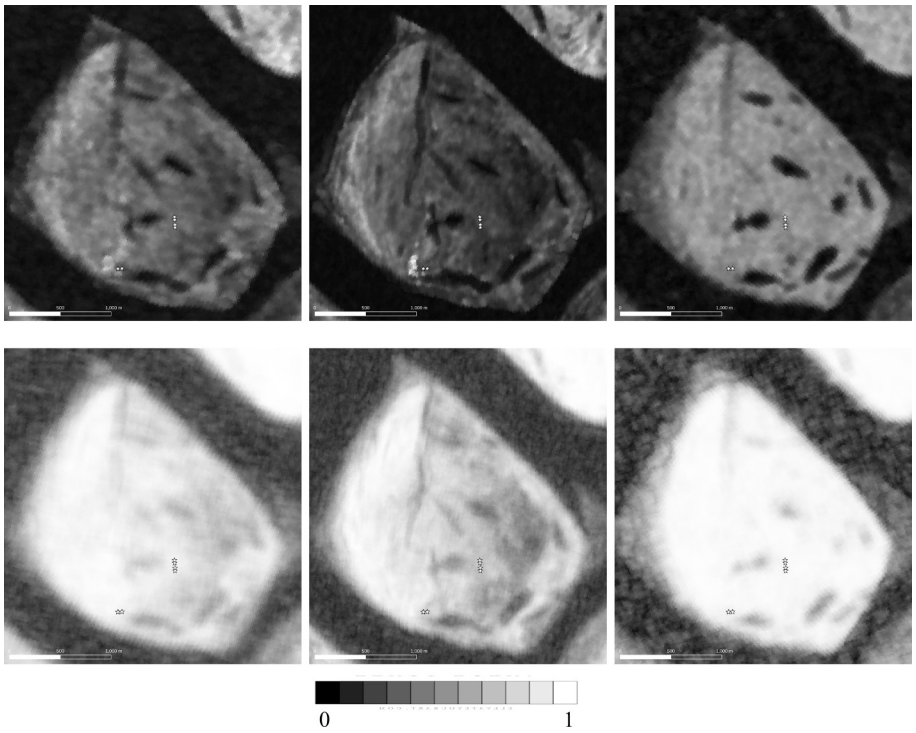

Fig. 5. Average coherence (first row) and average filtered interferogram correlation coefficient (second row) over 12 days for Sentinel-1 (left), 11 days for TerraSAR-X (middle) and 42/14 days for ALOS-2 PALSAR-2 (right) over Samoylov Island. The white stars indicate the locations of the in situ surface displacement measurement.

4.3. Habitat class map

Boxplots showing the total seasonal surface thaw displacement in 2018 across the habitat classes defined by Lisovski et al. (2025) for Sentinel-1, TerraSAR-X and ALOS-2 PALSAR-2 are shown in Fig. 7. *Sand*, *Water* and all land cover classes with a coverage of less than 1% within Samoylov Island are not considered in our analysis. We extracted the land cover classes per displacement product pixel and computed median values, interquartile range (25th–75th percentiles) and whiskers bound 5th and 95th percentiles.

The strongest seasonal thaw displacement is measured for all three sensors over class number 3 *Wet sedge communities* (covering 2.28% of the total area of the island), predominantly present on the floodplain in the West. Equally large displacement values are observed for class number 0 *Moist equisetum and shrub communities* (5.68%) and class number 2 *Moist to wet sedge complex* (13.22%), both also predominantly present on the floodplain in the West. The land cover classes on the floodplain showing the weakest displacement represent drier moisture regimes. Class number 7 *Sparsely vegetated areas* (4.25%), mainly present on the western tip of the floodplain, shows intermediate values. Class number 1 *Dry low shrub communities* (5.90%), on the dry ridges of the floodplain, has smaller displacements than the three moist to wet classes on the floodplain.

The land cover classes on the Holocene terrace show the smallest values of displacement with all three sensors. These include class number 4 *Polygonal tundra up to 50% surface water* (46.33%) and class number 5 *Polygonal tundra up to 20% surface water* (10.46%), both predominant in the eastern part of Samoylov Island, and class number 8 *Dry (tussock) tundra communities* (3.30%), found in particular on the border of the western part of the island. The more drained and degraded polygonal tundra class number 9 *Polygonal tundra up to 10% surface water* (1.97%), present along the margin between the eastern and western part of the island, is characterized by intermediate values of displacement.

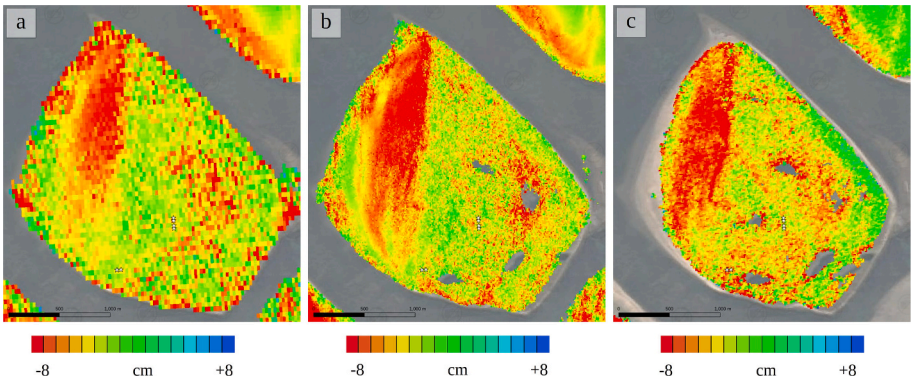

Fig. 6. Seasonal thaw displacement from Sentinel-1 between 12 June and 16 September 2018 (a), TerraSAR-X between 18 June and 14 September 2018 (b) and ALOS-2 PALSAR-2 between 12 June and 18 September 2018 (c) over Samoylov Island. The white stars indicate the locations of the in situ surface displacement measurements. Background image is Bing Aerial (©Microsoft).

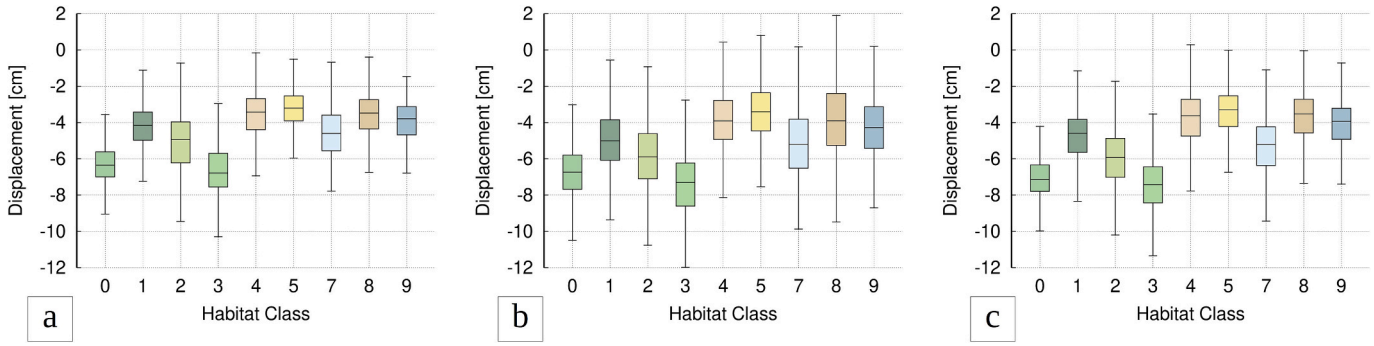

Fig. 7. Boxplots showing the seasonal thaw displacement in 2018 across the habitat classes for Sentinel-1 (a), TerraSAR-X (b) and ALOS-2 PALSAR-2 (c) over Samoylov Island. Sand, Water and habitat classes 6 and 10 with a coverage of less than 1% are not considered. The horizontal linework represents median values, boxes enclose interquartile range (25th–75th percentiles), and whiskers bound 5th and 95th percentiles. Outliers are not displayed. For the legend of the habitat classes see Fig. 3b.

5. Discussion

5.1. Coherence

We processed interferograms in series with time intervals of 12 days for Sentinel-1, 11 days for TerraSAR-X and 42/14 days for ALOS-2 PALSAR-2 images acquired during the summer season under snow-free conditions. In series interferograms provide consistent, coherent and correctly unwrapped input data necessary for the inversion to seasonal thaw displacement. Extending the temporal baselines to longer time intervals (e.g., 24 or 36 days for Sentinel-1 or 22 or 33 days for TerraSAR-X), as done for other applications to reduce the residues and better define the displacement rates (e.g., De Zan et al., 2015), was not feasible here. This is due to the rapid decrease in coherence caused by the pronounced subsidence and prominent vegetation and soil moisture conditions over low-land permafrost areas, in particular at the beginning of thawing (Fig. 4), also introducing challenges in phase unwrapping. Compared to the other two frequencies, the coherence decrease at L-Band is less pronounced, making a clearer distinction between open water and other land classes observable (Fig. 5). At C- and X-band the masking of open water is less successful and at these frequencies the coherence is also low between the western and eastern sectors of Samoylov Island, i.e., over *Wet sedge communities*.

5.2. Systematic phase bias

We are limiting the processing to high-coherent pairs with short temporal separation, knowing that short temporal, multi-looked and filtered interferograms tend to be biased. According to Ansari et al. (2021), the magnitude of the phase bias in each multi-looked interferogram may be deemed small, especially compared with the atmospheric perturbations. However, with the attenuation of atmospheric phase and the propagation of the interferogram phase bias within the time series, the corresponding error for the displacement velocity estimation is increasing. In their experiments with Sentinel-1 with a limitation of the temporal baseline at 72 days, Ansari et al. (2021) have observed biases of ~7 mm/a on distributed targets using temporal baselines of 6 days and noted that the bias is in general lower using temporal baselines of 12 days.

This bias can be understood observing the presence of closure phases (Zwieback et al., 2016; Ansari et al., 2021). Examining three subsequent images and building the closure phase, one typically finds inconsistencies in the order of a few degrees: scaling the error to the time span of a year the final deformation rate bias can easily reach several mm/a. Non-closure phase is caused by decorrelation noise and by sub-pixels changing scattering mechanisms and occurs because the multi-looking and filtering are independently carried out on each interferogram (De Luca et al., 2022). A possible physical interpretation of non-zero closure phase is related to moisture variations in semi-transparent media. The short term interferograms are biased because of the asymmetry of the moisture cycles combined with a non-linearity in the phase variations with respect to moisture.

In order to avoid systematic biases, Ansari et al. (2021) recommend a strategy primarily focused on excluding the short temporal baseline interferograms and using long baselines to decrease the overall phase errors. However, using long temporal baselines also decreases the coherence and thus the points where subsidence information can be retrieved, in particular over permafrost areas as on Samoylov Island

(Fig. 4). Exploiting the temporal data redundancy in large time series yields a degree of robustness of the phase-retrieval algorithms to such phase errors. De Luca et al. (2022) demonstrated e.g. that also short temporal baseline interferograms permit to guarantee a wide area coverage thanks to the large number of pixels with high temporal coherence values. De Luca et al. (2022) used a triangulation-based strategy for the evaluation of the "triangular coherence", the parameter used to select the pixels to be considered in the phase unwrapping procedure and in the subsequent steps of the Small Baseline Subset (SBAS) InSAR processing chain iterations, to retrieve the quasi-irrotational multi-look DInSAR phase components and, therefore, to prevent the presence of artifacts. Maghsoudi et al. (2022) developed a bias correction approach that uses the interferograms formed from the closest three connections, i.e., the biases in 6-day interferograms with those in 12-day and 18-day. This method is less sensitive to coherence loss as it only relies on the short term interferograms (6/12/18-day). Maghsoudi et al. (2022) noted that a similar approach could also be developed for areas where the revisit time for Sentinel-1 is 12 days.

Despite decreasing coherence with increasing temporal baseline (Fig. 4), we computed the cumulative phase closure using the set of multi-looked Sentinel-1 interferograms in a loop between 12 June and 16 September 2018, by subtracting the sum of the two 12-day interferograms from the 24-day interferogram. The cumulative phase bias, transformed to displacement in the LOS, over Samoylov Island amounts to −0.14 cm in 96 days. This would correspond to −0.52 cm/a, close to the typical values indicated by Ansari et al. (2021). However, −0.14 cm is still significantly smaller than the maximum seasonal LOS displacement of −4 cm observed over Samoylov Island.

We also computed the seasonal thaw displacement between 12 June and 16 September 2018 from consecutive 12 days intervals, consecutive 24 days intervals, consecutive 36 days intervals, and the stack of all these pairs (Supplementary Fig. 5), again despite rapidly decreasing coherence with time (Fig. 4). Over Samoylov Island the results are very consistent. The histogram of the difference between the 12 days and stacked solutions has its maximum at −0.2 cm (i.e., larger subsidence values are generated with short time intervals), again less than 5% of the maximum subsidence we observe in LOS over the island. Over a larger area the differences got larger, because of the noise in the 24 and 36 interferograms and errors in phase unwrapping as a consequence of the noise and the larger displacement over longer time period, in particular at the beginning of the thawing season. In our study, we therefore use carefully unwrapped, high-coherent pairs with the shortest temporal separation, even though we know that this may reduce accuracy with a possible systematic phase bias. However, the systematic phase bias is much lower than the maximum seasonal thaw displacement. To validate our results, we therefore compare the displacement maps at three different frequencies.

5.3. Intercomparison of seasonal thaw displacement at C-, X- and L-band

Scatter plots of the seasonal thaw displacement between the three different sensors are presented in Fig. 8. Only areas within the ALOS-2 PALSAR-2 mean filtered interferogram correlation coefficient above 0.5 were considered for this analysis. Maximum values of thaw displacements are on the order of −10 cm, minimum values are around 0 cm and the highest density of points is centered around 2–3 cm subsidence. No systematic bias between the three sensors towards large displacement is observed, with values following the identity line (i.e., 1:1).

The spread of the ALOS-2 PALSAR-2 values in the scatter plots is larger than that of Sentinel-1 and TerraSAR-X, as expected for the fewer number of available scenes at the longer wavelength. In all cases the dispersion is smaller than the typical error of DInSAR measurements estimated in previous works. Over urban areas, for instance, where a similarly high coherence over a multi-annual period is typically observed as in 12 days over low-land permafrost areas, an accuracy of 6–7 mm for single measurements at C-band was determined in a major validation project (Crosetto et al., 2009). This error is attributed partly to noise (e.g., 1–2 mm) and partly to tropospheric artifacts (e.g., 5–6 mm). Neglecting possible effects on the DInSAR phase by varying ionospheric, soil moisture, snow cover and vegetation conditions, inverting 8 Sentinel-1 12-days interferograms in series over one summer season results in a displacement precision of 3 to 6 mm (8/sqrt(8)*1–2 mm) for the noise and of 5 to 6 mm for the atmosphere (considering the first and last scenes only), i.e., a total of about 10 mm (Strozzi et al., 2018). This displacement value is slightly lower than those at the four locations assumed to be stationary used for the calibration of Sentinel-1 (cf. Section 3.1). Specifically, the measured displacements are 1.72 cm at Amerika Khaya on the Lena Delta, 0.29 cm at the Tiksi airport runway, and − 1.26 cm and − 1.14 cm at the two barren exposed surfaces at the southern margin on the mainland side. A similar precision of about 5% for the phase noise results in values about 1 mm at X-band and of about 6 mm at L-band. After inversion of 8 TerraSAR-X 11-days interferograms and 3 ALOS-2 PALSAR-2 42/14-days interferograms in series over one summer season, the expected displacement error due to phase noise is about 3 mm (8/sqrt(8)*1 mm) for TerraSAR-X and about 11 mm (3/sqrt(3)*6 mm) for ALOS-2 PALSAR-2. By adding tropospheric artifacts assumed to be similar at all wavelengths, e.g., 6 mm, we obtain a precision of about 9 mm for TerraSAR-X and of about 17 mm for ALOS-2 PALSAR-2.

5.4. In situ validation

A scatter plot of in situ versus satellite estimated seasonal thaw displacement in the summer of 2018 is presented in Fig. 9a. In situ seasonal thaw displacement was measured at SAM_1 to SAM_3 with metal pipes between 17 June and 7 September 2018 and at EO1 to EO4

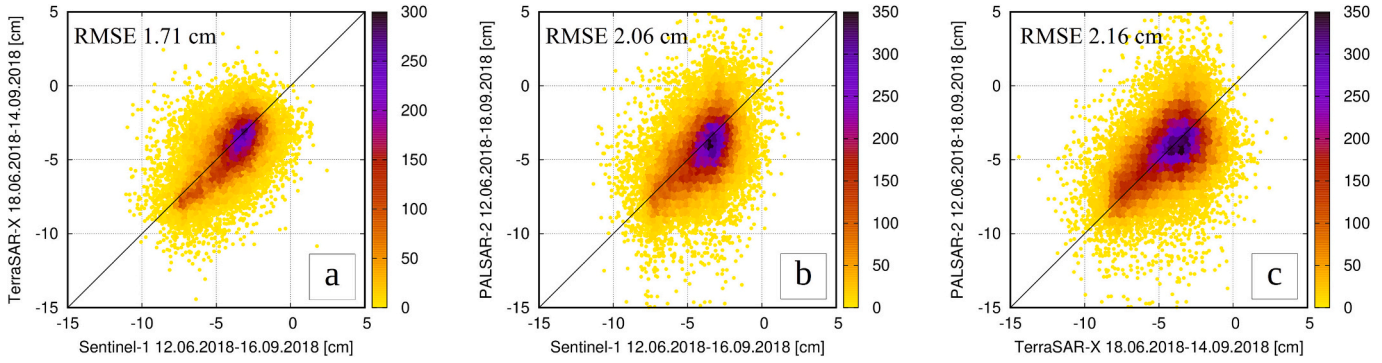

Fig. 8. Scatter plots of the seasonal thaw displacement in centimeters in 2018 over Samoylov Island from Sentinel-1 against TerraSAR-X (a), Sentinel-1 against ALOS-2 PALSAR-2 (b) and TerraSAR-X against ALOS-2 PALSAR-2 (c).

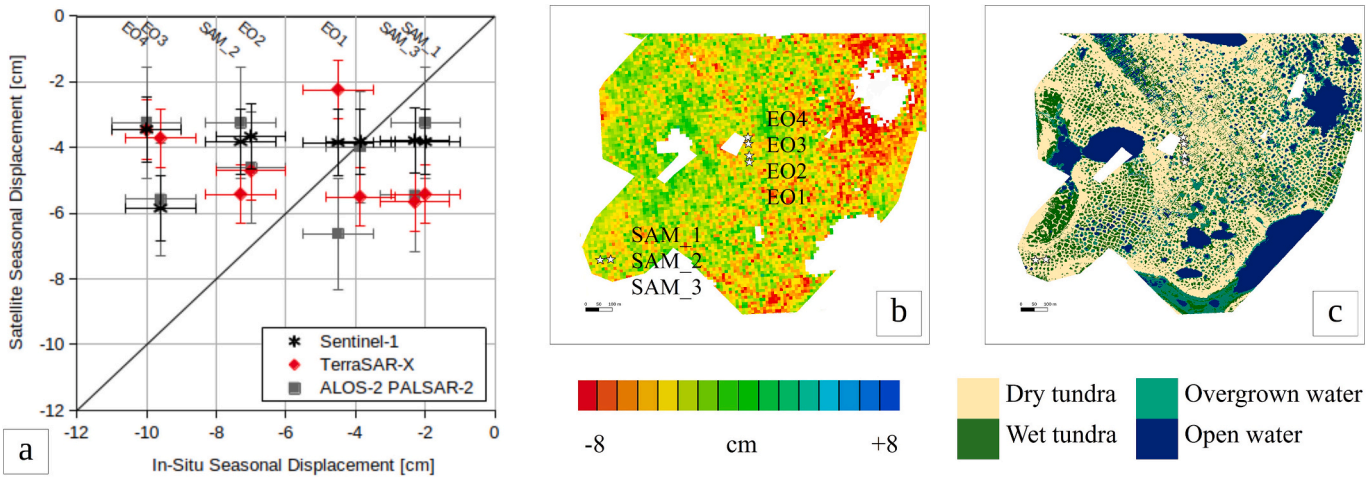

Fig. 9. (a) Scatter plot of in situ versus satellite estimated seasonal thaw displacement in the summer of 2018. Error bars are ±1 cm for Sentinel-1, ±0.9 cm for TerraSAR-X and ± 1.7 cm for ALOS-2 PALSAR-2 (cf. Section 5.3) and ± 1 cm for the in situ data (Antonova et al., 2018). (b) Seasonal thaw displacement from TerraSAR-X between 18 June and 14 September 2018. SAM_1 to SAM_3 are the three metal pipes measured on 17 June and 7 September 2018 (Fig. 2c). EO1 to EO4 are the four fiberglass poles measured on 16 June and 7 September 2018 (Fig. 2d). (c) Land cover classification of the ice-wedge polygonal tundra on Samoylov Island (Muster et al., 2012), showing the polygonal pattern of low-lying centers of wet tundra and polygonal ponds, separated by elevated polygonal rims of dry tundra.

with fiberglass poles between 16 June and 7 September 2018. Satellite seasonal thaw displacement was measured from Sentinel-1 between 12 June and 16 September 2018, from TerraSAR-X between 18 June and 14 September 2018 and from ALOS-2 PALSAR-2 between 12 June and 18 September 2018. SAM_1 to SAM_3 lie within a distance of 50 m, with SAM_1 and SAM_2 practically at the same location within a few meters distance, but with SAM_1 and SAM_3 on wet polygon centers and SAM_2 on a dry polygon rim (Fig. 2c). EO1 to EO4 are located within a distance of 100 m representing all three functional surface types of the polygonal tundra, i.e., dry, moist and wet (Figs. 2d).

Both in situ and satellite measurements indicate a pronounced downward movement of several centimeters, yet the values obtained in situ are larger. We note that such a comparison is challenging because the displacements measured in situ are point measurements, which can vary on a sub-meter scale within a range of several centimeters, i.e. on a much finer scale than the SAR resolution, depending on micro-topography, soil moisture and vegetation cover (Antonova et al., 2018). In particular, in situ measurements show that the dry polygon rim at SAM_2 subsides more than the wet polygon centers at SAM_1 and SAM_3. On the other hand, EO1 is installed on a dry polygon rim and subsides less then EO2 and EO3 installed towards the wet polygonal centers. EO4, however, which shows the highest in situ seasonal displacement is again installed on a dry polygon rim. The late summer Active Layer Thickness (ALT) measured on 7 September 2018 reveals no discernible pattern either. On the three SAM stations the ALT is moderately high, i.e. 60.0 cm at SAM_1, 71.3 cm at SAM_2 and 58.3 cm at SAM_3. For the two stations EO1 and EO2, the ALT is 26.0 cm and 30.5 cm, respectively, i.e. much lower that at the SAM stations. These values are also lower than the ALT of EO3 and EO4, with values of 42.0 cm and 37.0 cm, respectively.

Pronounced spatial variability of the seasonal thaw displacement is also observed from satellite data (Fig. 9b), but the agreement between DInSAR and local in situ measurements is weak. We explain this difference by several factors. First, when surface deformation is strongly correlated with temporal decorrelation, phase errors due to signal decorrelation can introduce a bias in the inferred deformation rates (Michaelides et al., 2019) and possibly errors in the phase unwrapping, which in turn lead to an underestimation of surface movement (Strozzi et al., 2018). Second, since in situ displacements can vary on a sub-metric scale within a range of several centimeters, when aggregated to satellite spatial resolution, the deformation exhibits less spatial variability at fine scales, leading to an underestimation of the actual displacement rates. Third, even if the in situ sites represent all three functional surface types of polygonal tundra, they still do not represent the area fraction when upscaled to the spatial resolution of the satellite. Therefore, it is very difficult to quantify isotropic thaw displacements with local point measurements except when a sufficiently larger number of samples has been collected to obtain a reliable mean value. Finally, we cannot exclude that the noise and atmospheric filters applied in our DInSAR processing chain also lead to an underestimation of motion.

5.5. *Connection to land cover and environmental dynamics*

The western part of Samoylov Island, represented by the floodplain and mainly covered by moist to wet land cover classes (Lisovski et al., 2025), clearly shows the largest thaw displacements (Fig. 6). Assuming that the dominant type of vegetation is related to the amount of soil moisture, as vegetation adjusts itself very well to differences in the ground conditions, the magnitude of the DInSAR-observed seasonal thaw subsidence is proportional to the ice/soil water content in the active layer. The correlation of high amplitude thaw subsidence with the wet ground in the west highlights a water availability control of the amplitude of the freeze and thaw cycles (Widhalm et al., 2025). Our results support previous results highlighting highest displacements on frost-susceptible sediments with high porosity (e.g Liu et al., 2010; Daout et al., 2017; Rouyet et al., 2019; Bartsch et al., 2019; Chen et al., 2020). Moisture levels on the polygonal tundra on Samoylov Island are spatially variable with a wet to dry soil moisture gradient within a few to tens of meters from a wet to moist polygonal center to dry polygonal rims (Fig. 9c). In addition, there are many polygonal ponds and a few larger water bodies in Samoylov Island's central part and dryer and well-drained areas towards its margins (Nitzbon et al., 2019). Here, we observe smaller thaw displacement values than over the floodplain and a large spatial variability, as discussed in the validation with in situ data (cf. Section 5.4). The polygonal wet tundra has many dry surfaces despite frequent ponds (Muster et al., 2012). This fits the measured low satellite-derived vertical movement, as the SAR signal in this region is largely influenced by dry rather than moist/wet surfaces for this land cover type.

In the middle of Samoylov Island, a NW to SE stripe of subsidence terminating before the fiberglass poles (EO1 to EO4) is clearly visible with ALOS-2 PALSAR-2 (Fig. 6c). This signal is weak in TerraSAR-X (Fig. 6b) and not recorded at all by Sentinel-1 (Fig. 6a) and corresponds to wet tundra in the land cover classification of Fig. 9c. We infer

that this signal is not recorded by Sentinel-1 due to of the sensor's lower spatial resolution. However, we cannot rule out differences in signal delay between the three wavelengths.

The water level above the surface was highest after snow melt at the end of May 2018, followed by drying in June, wetting in July and renewed drying in August. The time series of our DInSAR analyses are not detailed enough to determine whether water level fluctuations are reflected in the temporal changes in displacement. Shorter acquisition time intervals (e.g., 6 days as available over Svalbard and Greenland with Sentinel-1 between 2016 and 2021) would be required to record changes in the seasonal dynamics of the landscape (Rouyet et al., 2019).

Vegetation cover in different forms is extensive over Samoylov Island. Vegetation leaf out determined from time-lapse camera data started in late May before the DInSAR analyses. The higher than average June 2018 air temperature led to vascular vegetation shooting, i.e. green biomass growth, by mid June 2018, but vegetation shooting takes only a few days duration. An increasing delay from vegetation growth would increase the observed subsidence (e.g. Devlin and Lohman, 2025). However, the major effect of a vegetation layer on the DInSAR phase is a decrease in coherence, which we observe in particular when increasing the time interval of the interferograms and at higher frequencies (cf. Section 5.1). Also, the variability of movement within the SAR multi-look window leads to a decrease in coherence, which is stronger if the variability is not much smaller than the wavelength, i.e. at higher frequencies. Despite noticeable differences in coherence (Figs. 4 and 5) between Sentinel-1 and TerraSAR-X on one hand, and ALOS-2 PALSAR-2 on the other, the seasonal thaw displacement maps (Fig. 6) are similar.

6. Conclusions

We presented and compared seasonal thaw displacement maps for 2018 on Samoylov Island derived from Sentinel-1 (C-band), TerraSAR-X (X-band) and ALOS-2 PALSAR-2 (L-band). We observed a high spatial agreement of the derived summer surface subsidence maps at different frequencies over a terrain characterized by heterogeneous soil moisture and vegetation conditions. This suggests that surface motion is the predominant effect on the DInSAR phase compared to variations in soil moisture and vegetation conditions. There are at least three reasons for this. First, the magnitude of the interferometric phase delay caused by changing soil moisture conditions is expected to increase with the wavelength, as the penetration depth at lower frequencies is greater. However, at L-band there are no noticeable differences in the magnitude of the spatial distribution of motion. Second, despite the vegetation cover causing a stronger decrease of the coherence at higher frequencies, there are no noticeable differences in the magnitude of motion at X-band. Third, the dates of the SAR image acquisitions are different in the three datasets, i.e., they necessarily correspond to different environmental conditions. In spite of these differences, the agreement between the measurements of the seasonal thaw displacements derived at three different radar frequencies is very high both in their intercomparison (Fig. 8) and in the comparison with the habitat classes (Fig. 7).

The comparison with in situ measurements indicates a pronounced downward movement of several centimeters in both satellite and in situ data. However, as also observed in other case studies (e.g., Bartsch et al., 2019), the values obtained in situ are larger than those measured remotely. We argue that displacements measured in situ can vary on a sub-metric scale within a range of several centimeters depending on microtopography, soil moisture and vegetation cover, i.e., on scales finer than the SAR resolution. Therefore, when aggregated to the spatial resolution of the satellites, the deformation exhibits less spatial variability at the fine scale and an interferometric phase bias is introduced. However, we cannot rule out the possibility that the noise and atmospheric filters applied in our DInSAR processing chain may also introduce an underestimation of motion. For future work, we could consider calculating the differential interferograms for all three sensors with the same spatial resolution. This could help to isolate the effects of frequency changes. Future work could also include local processing at full resolution within the island to verify whether the differences from the in situ data decrease. Additionally, a statistical characterization of the properties of sub-SAR pixels using high-resolution optical data (UAV, aerial imagery) could be helpful in understanding the statistics (microtopography, polygonal water bodies, vegetation) that feed into an InSAR pixel deformation estimate. Also InSAR measurements with higher spatial resolution have the potential to monitor the displacement and geomorphological processes of individual periglacial landforms (e.g. Spotlight Mode data with a resolution of 1 m, Short et al., 2024). The in situ observations on air temperature, ground temperature, snow depth, water level above the surface, thaw depths of the active layer and time-lapse camera observations could be linked to the analysis of 12-day coherence for further possible extended interpretations. For future in situ measurements to validate satellite records, we suggest, if feasible, installing sensor grids within a satellite resolution cell of about 20 m on different types of terrain, possibly in areas where satellite observations have indicated pronounced differences in the seasonal signal.

The results of the three seasonal thaw displacement maps over a larger section of the central part of the Lena Delta, presented in supplementary Fig. 4, show less consistent patterns between the three sensors than over Samoylov Island. This suggests that our current analysis only works for a relatively small area (~5 km^2) and that it is difficult to extend it to a larger region due to decorrelation and tropospheric noise. In order to work on a larger scale, suitable atmospheric filtering must be investigated, as simple spatial filtering can suppress large-scale permafrost-related subsidence signals and lead to the underestimation of displacement values (Widhalm et al., 2025). The Generic Atmospheric Correction Online Service (GACOS) for DInSAR (Yu et al., 2018) or the Extended Timing Annotation Dataset (ETAD) for Sentinel-1 are promising assets in this regard (Gisinger et al., 2022). They can be considered in future work to check whether consistency between in situ and remote sensing measurements or InSAR observations from two sensors can be improved over a larger overlap area to further demonstrate the potential and challenges of the technique over remote Arctic regions. In addition, due to the significant presence of different land cover types within the delta region, each category likely responds differently to seasonal thaw displacement and radar signal interaction. Therefore, it is essential to conduct targeted, separate investigations for each major land cover type to accurately quantify their distinct impacts on both InSAR decorrelation and ground surface displacement.

In this contribution we analyzed SAR data of the thawing season 2018. With a longer time series of data over multiple years, long-term changes in seasonal signals as well as the long-term rate of subsidence can be analyzed. The long-term component of the deformation is related to the ice content at the top of the permafrost, therefore DInSAR can be employed to document permafrost degradation or aggregation. Over the Lena Delta, this is feasible with Sentinel-1 only from July 2016 until December 2021, as no more IW mode images were acquired over northern Siberia since the failure of Sentinel-1B on 23 December 2021. TerraSAR-X data are only regularly acquired over the central part of the Lena Delta but not for the entire delta. ALOS-2 PALSAR-2 data are acquired only sporadically over the Lena Delta, making a long-term DInSAR time series analysis particularly challenging. For possible future synergistic use of C-, X-, and L-band data for the monitoring of summer and multi-annual surface deformation in low-land permafrost areas, the Sentinel-1 satellite constellation is complemented by two additional C-band sensors (Sentinel-1C and -1D). X-band sensors are being commissioned not only by public agencies but also, since 2018, by private companies (e.g., ICEYE, Capella Space and Umbra Space). New sensors at L-band were recently launched by JAXA (ALOS-4 PALSAR-3) and NASA (NISAR) or are currently being developed at ESA (ROSE-L).

The habitat class analysis suggests that the DInSAR seasonal deformation might document the spatial variability of the moisture content in the active layer. DInSAR time-series therefore have the potential to

improve the characterization of subsurface hydrogeological and thermal parameters used in permafrost models to simulate the ground thermal regime (Westermann et al., 2023). This would allow to improve the performance of permafrost models to simulate ground temperature, ALT and permafrost distribution at local and regional scales (Obu et al., 2019). Model parametrization could also support soil moisture estimation from the amplitude and temporal progression of the seasonal thaw displacement to complement other soil moisture retrieval algorithms that utilize DInSAR closure phase and decorrelation phase (Zwieback et al., 2017; De Zan and Gomba, 2018; Michaelides et al., 2019). The potential influence of soil moisture content on radar backscatter at a specific polarization, which differs in our study between Sentinel-1 on the one hand and TerraSAR-X and ALOS-2 PALSAR-2 on the other, may be subject to future investigation.

CRediT authorship contribution statement

Tazio Strozzi: Writing – review & editing, Writing – original draft, Visualization, Methodology, Formal analysis, Data curation, Conceptualization. **Nina Jones:** Writing – original draft, Data curation. **Julia Boike:** Writing – review & editing, Validation, Investigation. **Sofia Antonova:** Writing – review & editing, Validation. **Birgit Heim:** Writing – review & editing, Validation, Formal analysis. **Silvan Leinss:** Writing – review & editing, Formal analysis. **Urs Wegmüller:** Writing – review & editing, Supervision, Formal analysis. **Sebastian Westermann:** Writing – review & editing, Supervision, Conceptualization. **Andreas Kääb:** Writing – review & editing, Supervision, Conceptualization. **Guido Grosse:** Writing – review & editing, Validation. **Annett Bartsch:** Writing – review & editing, Funding acquisition, Conceptualization.

Funding

This research has been supported by the European Space Agency CCI Permafrost Project (grant no. 4000123681/18/I-NB).

Declaration of competing interest

The authors declare that the research was conducted in the absence of any commercial or financial relationships that could be construed as a potential conflict of interest.

Acknowledgments

Sentinel-1 images available from Copernicus. TerraSAR-X data are courtesy of LAN3847, copyright DLR. ALOS-2 PALSAR-2 data are courtesy of RA6_3016, copyright JAXA. TanDEM-X data are courtesy of DEM_GEOL1365, copyright DLR. We thank Paula Olea (CTTC) for helping in the Sentinel-1 processing.

Appendix A. Supplementary data

Supplementary data to this article can be found online at https://doi.org/10.1016/j.rse.2026.115293.

Data availability

Data will be made available on request.

References

Ansari, H., De Zan, F., Parizzi, A., 2021. Study of systematic bias in measuring surface deformation with SAR interferometry. IEEE Trans. Geosci. Remote Sens. 59, 1285–1301.

Antonova, S., Sudhaus, H., Strozzi, T., Zwieback, S., Kääb, A., Heim, B., Langer, M., Bornemann, N., Boike, J., 2018. Thaw subsidence of a Yedoma landscape in northern Siberia, measured in situ and estimated from TerraSAR-X interferometry. Remote Sens. 10, 494.

Are, F., Reimnitz, E., 2000. An overview of the Lena River Delta setting: geology, tectonics, geomorphology, and hydrology. J. Coast. Res. 16 (4), 1083–1093.

Ballantyne, C.K., 2018. Periglacial Geomorphology. John Wiley & Sons, Ltd, Hoboken, NJ, p. 454.

Bamler, R., Hartl, P., 1998. Synthetic aperture radar interferometry. Inverse Probl. 14, R1–R54.

Bartsch, A., Leibman, M., Strozzi, T., Khomutov, A., Widhalm, B., Babkina, E., Mullanurov, D., Ermokhina, K., Kroisleitner, C., Bergstedt, H., 2019. Seasonal progression of ground displacement identified with satellite radar interferometry and the impact of unusually warm conditions on permafrost at the Yamal peninsula in 2016. Remote Sens. 11, 1865.

Berardino, P., Fornaro, G., Lanari, R., Sansosti, E., 2002. A new algorithm for surface deformation monitoring based on small baseline differential SAR interferograms. IEEE Trans. Geosci. Remote Sens. 40, 2375–2383.

Boike, J., Kattenstroth, B., Abramova, K., Bornemann, N., Chetverova, A., Fedorova, I., Fröb, K., Grigoriev, M., Grüber, M., Kutzbach, L., Langer, M., Minke, M., Muster, S., Piel, K., Pfeiffer, E.-M., Stoof, G., Westermann, S., Wischnewski, K., Wille, C., Hubberten, H.-W., 2013. Baseline characteristics of climate, permafrost and land cover from a new permafrost observatory in the Lena River Delta, Siberia (1998–2011). Biogeosciences 10, 2105–2128.

Boike, J., Veh, G., Viitanen, L.-K., Bornemann, N., Stoof, G., Muster, S., 2015. Visible and near-infrared orthomosaic of Samoylov Island, Siberia, summer 2015 (5.3 GB). In: PANGAEA.

Boike, J., Nitzbon, J., Anders, K., Grigoriev, M., Bolshiyanov, D., Langer, M., Lange, S., Bornemann, N., Morgenstern, A., Schreiber, P., Wille, C., Chadburn, S., Gouttevin, I., Burke, E., Kutzbach, L., 2018. Time lapse camera pictures at Samoylov, LTO, 2002-2017. In: PANGAEA.

Boike, J., Nitzbon, J., Anders, K., Grigoriev, M., Bolshiyanov, D., Langer, M., Lange, S., Bornemann, N., Morgenstern, A., Schreiber, P., Wille, C., Chadburn, S., Gouttevin, I., Burke, E., Kutzbach, L., 2019. A 16-year record (2002–2017) of permafrost, active-layer, and meteorological conditions at the Samoylov Island Arctic permafrost research site, Lena River delta, northern Siberia: an opportunity to validate remote-sensing data and land surface, snow, and permafrost models. Earth Syst. Sci. Data 11, 261–299.

Boike, J., Wille, C., Bolshiyanov, D., Bornemann, N., Grigoriev, M., Grünberg, I., Miesner, F., 2022. Continuous measurements in soil and air at the permafrost long-term observatory at Samoylov Station (2002 et seq). In: PANGAEA.

Brancato, V., Hajnsek, I., 2018. Analyzing the influence of wet biomass changes in polarimetric differential SAR interferometry at L-band. IEEE J. Sel. Top. Appl. Earth Obs. Remote Sens. 11, 1494–1508.

Chen, J., Wu, Y., O'Connor, M., Cardenas, M.B., Schaefer, K., Michaelides, R., Kling, G., 2020. Active layer freeze-thaw and water storage dynamics in permafrost environments inferred from InSAR. Remote Sens. Environ. 248, 112007.

Costantini, M., 1998. A novel phase unwrapping method based on network programming. IEEE Trans. Geosci. Remote Sens. 36, 813–821.

Crosetto, M., Monserrat, O., Bremmer, C., Hanssen, R., Capes, R., Marsh, S., 2009. Ground motion monitoring using SAR interferometry: quality assessment. Eur. Geol. 26, 12–15.

Daout, S., Doin, M.P., Peltzer, G., Socquet, A., Lasserre, C., 2017. Large-scale InSAR monitoring of permafrost freeze-thaw cycles on the Tibetan Plateau. Geophys. Res. Lett. 44, 901–909.

De Luca, C., Casu, F., Manunta, M., Onorato, G., Lanari, R.: Comments on "study of systematic bias in measuring surface deformation with SAR interferometry". IEEE Transactions on Geoscience and Remote Sensing, vol. 60, pp. 1–5, 2022, Art no. 9100505, doi:https://doi.org/10.1109/TGRS.2021.3103037.

De Zan, F., Gomba, G., 2018. Vegetation and soil moisture inversion from SAR closure phases: first experiments and results. Remote Sens. Environ. 217 (November), 562–572.

De Zan, F., Monti-Guarnieri, A., 2006. TOPSAR: terrain observation by progressive scans. IEEE Trans. Geosci. Remote Sens. 44, 2352–2360.

De Zan, F., Parizzi, A., Prats-Iraola, P., López-Dekker, P., 2014. A SAR interferometric model for soil moisture. IEEE Trans. Geosci. Remote Sens. 52, 418–425.

De Zan, F., Zonno, M., López-Dekker, P., 2015. Phase inconsistencies and multiple scattering in SAR interferometry. IEEE Trans. Geosci. Remote Sens. 53, 6608–6616.

Devlin, K.R., Lohman, R.B., 2025. Evaluation of vegetation bias in InSAR time series for agricultural areas within the San Joaquin Valley, CA. Earth Space Sci. 12, e2024EA004062. https://doi.org/10.1029/2024EA004062.

Eshqi Molan, Y., Lu, Z., 2020. Modeling InSAR phase and SAR intensity changes induced by soil moisture. IEEE Trans. Geosci. Remote Sens. 58, 4967–4975.

French, H.M., 2007. The Periglacial Environment, 3rd ed. John Wiley & Sons, Ltd, West Sussex, UK.

Gisinger, C., Libert, L., Marinkovic, P., Krieger, L., Larsen, Y., Valentino, A., Breit, H., Balss, U., Suchandt, S., Nagler, T., Eineder, M., Miranda, N., 2022. The extended timing annotation dataset for Sentinel-1—product description and first evaluation results. IEEE Trans. Geosci. Remote Sens. 60, 1–22. https://doi.org/10.1109/TGRS.2022.3194216, 5232622.

Goldstein, R.M., Werner, C.L., 1998. Radar interferogram filtering for geophysical applications. Geophys. Res. Lett. 25, 4035–4038.

Gomba, G., Parizzi, A., De Zan, F., Eineder, M., Bamler, R., 2016. Toward operational compensation of ionospheric effects in SAR interferograms: the split-spectrum method. IEEE Trans. Geosci. Remote Sens. 54, 1446–1461.

Guneriussen, T., Hogda, K.A., Johnsen, H., Lauknes, I., 2001. InSAR for estimation of changes in snow water equivalent of dry snow. IEEE Trans. Geosci. Remote Sens. 39, 2101–2108.

Günther, F., Overduin, P.P., Yakshina, I.A., Opel, T., Baranskaya, A.V., Grigoriev, M.N., 2015. Observing Muostakh disappear: permafrost thaw subsidence and erosion of a

ground-ice-rich island in response to arctic summer warming and sea ice reduction. Cryosphere 9, 151–178.
Hanssen, R., 1998. Atmospheric heterogeneities in ERS tandem SAR interferometry. In: DEOS Report No 98.1. Delft University Press, Delft, The Netherlands, p. 155. ISBN 90-407-1774-5 / CIP.
Heim, B., Lisovski, S., Wieczorek, M., Morgenstern, A., Juhls, B., Shevtsova, I., Kruse, S., Boike, J., Fedorova, I., Herzschuh, U., 2022. Spring snow cover duration and tundra greenness in the Lena Delta, Siberia: two decades of MODIS satellite time series (2001−2021). Environ. Res. Lett. 17, 085005.
Juhls, B., Stedmon, C., Morgenstern, A., Meyer, H., Hölemann, J., Heim, B., Povazhnyi, V., Overduin, P.P., 2020. Identifying drivers of seasonality in Lena River biogeochemistry and dissolved organic matter fluxes. Front. Environ. Sci. 8.
Kartoziia, A., 2019. Assessment of the ice wedge polygon current state by means of UAV imagery analysis (Samoylov Island, the Lena Delta). Remote Sens. 11, 1627. https://doi.org/10.3390/rs11131627.
Lisovski, S., Runge, A., Shevtsova, I., Landgraf, N., Morgenstern, A., Okoth, R.R., Fuchs, M., Lashchinskiy, N., Stadie, C., Beamish, A., Herzschuh, U., Grosse, G., Heim, B., 2025. A new habitat map of the Lena Delta in Arctic Siberia based on field and remote sensing datasets. Earth Syst. Sci. Data Discuss. 17, 1707–1730. https://doi.org/10.5194/essd-17-1707-2025.
Liu, L., Zhang, T., Wahr, J., 2010. InSAR measurements of surface deformation over permafrost on the North Slope of Alaska. J. Geophys. Res. 115, F03023.
Maghsoudi, Y., Hooper, A., Wright, T., Lazecky, M., Ansari, H., 2022. Characterizing and correcting phase biases in short-term, multilooked interferograms. Remote Sens. Environ. 275, 113022. ISSN 0034-4257. https://doi.org/10.1016/j.rse.2022.113022.
Michaelides, R., Zebker, H., Zheng, Y., 2019. An algorithm for estimating and correcting decorrelation phase from InSAR data using closure phase triplets. IEEE Trans. Geosci. Remote Sens. 57, 10390–10397.
Michaelides, R., Chen, R., Zhao, Y., Schaefer, K., Parsekian, A., Sullivan, T., Moghaddam, M., Zebker, H., Liu, L., Xu, X., Chen, J., 2021. Permafrost dynamics observatory—part I: postprocessing and calibration methods of UAVSAR L-band InSAR data for seasonal subsidence estimation. Earth Space Sci. 8, e2020EA001630.
Morgenstern, A., Grosse, G., Günther, F., Fedorova, I., Schirrmeister, L., 2011. Spatial analyses of thermokarst lakes and basins in Yedoma landscapes of the Lena Delta. Cryosphere 5, 849–867.
Morgenstern, A., Ulrich, M., Günther, F., Roessler, S., Fedorova, I., Rudaya, N., Wetterich, S., Boike, J., Schirrmeister, L., 2013. Evolution of thermokarst in East Siberian ice-rich permafrost: a case study. Geomorphology 201, 363–379.
Morgenstern, A., Heim, B., Hainbach, T., 2021. Time Lapse Camera videos for monitoring snow and vegetation evolution in 2018 on Samoylov and Kurungnakh islands, Lena Delta, Russia. In: PANGAEA.
Morrison, K., Bennett, J.C., Nolan, M., Menon, R., 2011. Laboratory measurement of the DInSAR response to spatiotemporal variations in soil moisture. IEEE Trans. Geosci. Remote Sens. 49, 3815–3823.
Muster, S., Langer, M., Heim, B., Westermann, S., Boike, J., 2012. Subpixel heterogeneity of ice-wedge polygonal tundra: a multi-scale analysis of land cover and evapotranspiration in the Lena River Delta, Siberia. Tellus Ser. B 64, 17301.
Nitzbon, J., Langer, M., Westermann, S., Martin, L., Aas, K.S., Boike, J., 2019. Pathways of ice-wedge degradation in polygonal tundra under different hydrological conditions. Cryosphere 13, 1089–1123.
Nolan, M., Fatland, D.R., Hinzman, L., 2003. DInSAR measurement of soil moisture. IEEE Trans. Geosci. Remote Sens. 41, 2802–2813.
Nyland, K., Shiklomanov, N., Streletskiy, D., Nelson, F., Klene, A., Kholodov, A., 2021. Long-term Circumpolar Active Layer Monitoring (CALM) program observations in Northern Alaskan tundra. Polar Geogr. 44, 167–185.
Obu, J., Westermann, S., Bartsch, A., Berdnikov, N., Christiansen, H.H., Dashtseren, A., Delaloye, R., Elberling, B., Etzelmüller, B., Kholodov, A., Khomutov, A., Kääb, A., Leibman, M.O., Lewkowicz, A.G., Panda, S.K., Romanovsky, V., Way, R.G., Westergaard-Nielsen, A., Wu, T., Yamkhin, J., Zou, D., 2019. Northern hemisphere permafrost map based on TTOP modelling for 2000-2016 at 1 km2 scale. Earth Sci. Rev. 193, 299–316.
Pitz, W., Miller, D., 2010. The TerraSAR-X satellite. IEEE Trans. Geosci. Remote Sens. 48, 615–622.
Polyakov, V., Kartoziia, A., Nizamutdinov, T., Wang, W., Abakumov, E., 2022. Soil-geomorphological mapping of Samoylov Island based on UAV imaging. Front. Environ. Sci. 10. https://doi.org/10.3389/fenvs.2022.948367.
Rosen, P., Hensley, S., Joughin, I., Li, F., Madsen, S., Rodriguez, E., Goldstein, R., 2000. Synthetic aperture radar interferometry. Proc. IEEE 88, 333–382.
Rouyet, L., Lauknes, T.R., Christiansen, H.H., Strand, S.M., Larsen, Y., 2019. Seasonal dynamics of a permafrost landscape, Adventdalen, Svalbard, investigated by InSAR. Remote Sens. Environ. 231, 111236.
Rouyet, L., Liu, L., Strand, S.M., Christiansen, H.H., Lauknes, T.R., Larsen, Y., 2021. Seasonal InSAR displacements documenting the active layer freeze and thaw progression in Central-Western Spitsbergen, Svalbard. Remote Sens. 13, 2977.
Sandwell, D., Price, E., 1998. Phase gradient approach to stacking interferograms. J. Geophys. Res. Solid Earth 103 (B12), 30183–30204.
Sarabandi, K., Azadegan, R., 2000. Simulation of interfrometric SAR response to rough surfaces covered with a dielectric layer. In: IEEE IGARSS, pp. 1739–1741.
Schaefer, K., Liu, L., Parsekian, A., Jafarov, E., Chen, A., Zhang, T.J., Gusmeroli, A., Panda, S., Zebker, H., Schaefer, T., 2015. Remotely sensed active layer thickness (ReSALT) at Barrow, Alaska using interferometric synthetic aperture radar. Remote Sens. 7, 3735–3759.
Scheer, J., Caduff, R., How, P., Marcer, M., Strozzi, T., Bartsch, A., Ingeman-Nielsen, T., 2023. Thaw-season InSAR surface displacements and frost susceptibility mapping to support community-scale planning in Ilulissat, West Greenland. Remote Sens. 15, 3310.
Schwamborn, G., Rachold, V., Grigoriev., 2002. Late quaternary sedimentation history of the Lena Delta. Quat. Int. 89, 119–134.
Shiklomanov, N.I., Streletskiy, D.A., Little, J.D., Nelson, F.E., 2013. Isotropic thaw subsidence in undisturbed permafrost landscapes. Geophys. Res. Lett. 40, 6356–6361.
Short, N., Brisco, B., Couture, N., Pollard, W., Murnaghan, K., Budkewitsch, P., 2011. A comparison of TerraSAR-X, RADARSAT-2 and ALOS-PALSAR interferometry for monitoring permafrost environments, case study from Herschel Island, Canada. Remote Sens. Environ. 115, 3491–3506.
Short, N., LeBlanc, A.-M., Sladen, W., Oldenborger, G., Mathon-Dufour, V., Brisco, B., 2014. RADARSAT-2 D-InSAR for ground displacement in permafrost terrain, validation from Iqaluit Airport, Baffin Island, Canada. Remote Sens. Environ. 141, 40–51.
Short, N., Charbonneau, F., Fraser, R., 2024. Unique contributions of the RADARSAT missions to InSAR monitoring of permafrost terrain. In: Proc. 12th International Conference on Permafrost, Whitehorse, Yukon, Canada.
Streletskiy, D.A., Maslakov, A., Grosse, G., Shiklomanov, N.I., Farquharson, L., Zwieback, S., Iwahana, G., Bartsch, A., Liu, L., Strozzi, T., Lee, H., Debolskiy, M.V., 2025. Thawing permafrost is subsiding in the Northern Hemisphere—review and perspectives. Environ. Res. Lett. 20, 013006. https://doi.org/10.1088/1748-9326/ada2ff.
Strozzi, T., Wegmüller, U., Matzler, C., 1999. Mapping wet snowcovers with SAR interferometry. Int. J. Remote Sens. 20, 2395–2403.
Strozzi, T., Antonova, S., Günther, F., Mätzler, E., Vieira, G., Wegmüller, U., Westermann, S., Bartsch, A., 2018. Sentinel-1 SAR interferometry for surface deformation monitoring in low-land permafrost areas. Remote Sens. 10, 1360.
Suzuki, S., Kankaku, Y., Shimada, M., 2013. ALOS-2 acquisition strategy. In: IEEE IGARSS, pp. 2412–2415.
Torres, R., Snoeij, P., Geudtner, D., Bibby, D., Davidson, M., Attema, E., Potin, P., Rommen, B., Floury, N., Brown, M., et al., 2012. GMES Sentinel-1 mission. Remote Sens. Environ. 120, 9–24.
Wang, L., Marzahn, P., Bernier, M., Jacome, A., Poulin, J., Ludwig, R., 2017. Comparison of TerraSAR-X and ALOS PALSAR differential interferometry with multisource DEMs for monitoring ground displacement in a discontinuous permafrost region. IEEE J. Sel. Top. Appl. Earth Obs. Remote Sens. 10, 4074–4093.
Wang, C., Zhang, Z., Zhang, H., Zhang, B., Tang, Y., Wu, Q., 2018. Active layer thickness retrieval of Qinghai–Tibet permafrost using the TerraSAR-X InSAR technique. IEEE J. Sel. Top. Appl. Earth Obs. Remote Sens. 11, 4403–4413.
Wegmüller, U., Werner, C., 1995. SAR interferometric signatures of forest. IEEE Trans. Geosci. Remote Sens. 33, 1153–1161.
Wegmuller, U., Werner, C., 1997. Retrieval of vegetation parameters with SAR interferometry. IEEE Trans. Geosci. Remote Sens. 35, 18–24. https://doi.org/10.1109/36.551930.
Werner, C., Wegmüller, U., Strozzi, T., 2012. Deformation time-series of the Lost-Hills oil field using a multi-baseline interferometric SAR inversion algorithm with finite difference smoothing constraints. In: Proceedings of the AGU Fall Meeting, San Francisco, CA, USA, 3–7 December 2012.
Wessel, B., Huber, M., Wohlfart, C., Marschalk, U., Kosmann, D., Roth, A., 2018. Accuracy assessment of the global TanDEM-X Digital Elevation Model with GPS data. ISPRS J. Photogr. Rem. Sens. 139, 171–182.
Westerhoff, R., Steyn-Ross, M., 2020. Explanation of InSAR phase disturbances by seasonal characteristics of soil and vegetation. Remote Sens. 12, 3029.
Westermann, S., Ingeman-Nielsen, T., Scheer, J., Aalstad, K., Aga, J., Chaudhary, N., Etzelmüller, B., Filhol, S., Kääb, A., Renette, C., Schmidt, L.S., Schuler, T.V., Zweigel, R.B., Martin, L., Morard, S., Ben-Asher, M., Angelopoulos, M., Boike, J., Groenke, B., Miesner, F., Nitzbon, J., Overduin, P., Stuenzi, S.M., Langer, M., 2023. The CryoGrid community model (version 1.0) – a multi-physics toolbox for climate-driven simulations in the terrestrial cryosphere. Geosci. Model Dev. 16, 2607–2647.
Widhalm, B., Bartsch, A., Strozzi, T., Jones, N., Khomutov, A., Babkina, E., Leibman, M., Khairullin, R., Göckede, M., Bergstedt, H., von Baeckmann, C., Muri, X., 2025. InSAR-derived seasonal subsidence reflects spatial soil moisture patterns in Arctic lowland permafrost regions. Cryosphere 19, 1103–1133. https://doi.org/10.5194/tc-19-1103-2025.
Xiao, R., Yu, C., Li, Z., He, X., 2021. Statistical assessment metrics for InSAR atmospheric correction: applications to generic atmospheric correction online service for InSAR (GACOS) in Eastern China. Int. J. Appl. Earth Obs. Geoinf. 96, 102289.
Yu, C., Li, Z., Penna, N.T., Crippa, P., 2018. Solid earth generic atmospheric correction model for interferometric synthetic aperture radar observations. J. Geophys. Res. 123, 9202–9222.
Zhang, H., Wang, C., Tang, Y., Zhang, B., Wu, F., Wang, J., Zhang, Z., 2020. Active layer thickness retrieval over the Qinghai-Tibet plateau using Sentinel-1 multitemporal InSAR monitored permafrost subsidence and temporal-spatial multilayer soil moisture data. IEEE Access 8, 84336–84351.
Zink, M., Moreira, A., 2014. TanDEM-X mission status: the new topography of the earth takes shape. In: IEEE IGARSS, pp. 3386–3389.
Zwieback, S., Liu, X., Antonova, S., Heim, B., Bartsch, A., Boike, J., Hajnsek, I., 2016. A statistical test of phase closure to detect influences on DInSAR deformation estimates besides displacements and decorrelation noise: two case studies in high-latitude regions. IEEE Trans. Geosci. Remote Sens. 54 (9), 5588–5601. https://doi.org/10.1109/TGRS.2016.2569435.
Zwieback, S., Hensley, S., Hajnsek, I., 2017. Soil moisture estimation using differential radar interferometry: toward separating soil moisture and displacements. IEEE Trans. Geosci. Remote Sens. 55, 5069–5083.